



Enhanced photocatalytic hydrogen peroxide production at a solid-liquid-air interface via microenvironment engineering

Lei Chen^{a,b}, Shan Li^{a,b}, Zhi Yang^{a,b}, Cheng Chen^{a,b}, Chiheng Chu^{a,b}, Baoliang Chen^{a,b,*}

^a Department of Environmental Science, Zhejiang University, Hangzhou, Zhejiang 310058, China

^b Zhejiang Provincial Key Laboratory of Organic Pollution Process and Control, Hangzhou 310058, China

ARTICLE INFO

Keywords:

Photocatalysis
Hydrogen peroxide
Triphase
Microenvironment engineering
Graphitic carbon nitride

ABSTRACT

Photocatalytic oxygen reduction is a promising strategy to generate H₂O₂ in a low-energy input and more sustainable way. Despite great progress have made in photocatalyst design, the rate-limiting step that poor accessibility of the O₂ to photocatalysts in water remains unexplored. Here, we design a solid-liquid-air triphasic interface over a melamine foam to boost the interfacial O₂ transportation. A Wenzel-Cassie state coexists in a hydrophobic interface and form a tubular confined space with a thickness of 100 μm, which allows the O₂ directly transferred to the photocatalyst from the air, greatly boost the formation of H₂O₂. In addition, a tubular confined microenvironment formed on the surface greatly enhances oxygen diffusion, and suppressed the unwanted decomposition of H₂O₂. This surface microenvironment engineering resulted in a 10-fold enhancement in the photosynthesis H₂O₂ compared to the traditional solid-liquid diphasic system, pinpointing the necessary O₂ mass diffusion for photocatalytic H₂O₂ generation.

1. Introduction

Hydrogen peroxide (H₂O₂) is a versatile and clean oxidant and widely used in wastewater remediation [1–3], chemical industry [4,5], fuel cell [6–8], and disinfection [9–11]. So far, the energy- and waste-intensive anthraquinone (AQ) process is still accounted for more than 95% in H₂O₂ production [1,12]. The deficiencies of the AQ process are motivating to develop alternative synthesis methods in a low-energy input and more sustainable way [13–15]. The photocatalytic oxygen reduction, as a green process, can proceed by a two-electron process (2e⁻ ORR) to generate H₂O₂ (O₂ + 2e⁻ + 2H⁺ → H₂O₂, O₂/H₂O₂ = 0.695 V vs. NHE), which has garnered huge attention as it just requires water and oxygen as the basic building materials [16–18].

Until now, most of the research has focused on the properties of photocatalysts, such as the selectivity of oxygen reduction [19–21], photogenerated electron transfer and separation [5,16,22,23] to realize the synthesis of H₂O₂ via the 2e⁻ ORR process while maintaining high photocatalytic activity. Generally, the photocatalytic synthesis of H₂O₂ is carried out in a solid-liquid diphasic environment (Scheme 1a) with O₂ bubbling into solution [24–26]. The product concentration of H₂O₂ is still largely retarded. The low production of H₂O₂ can be attributed to the following aspects. First, in the diphasic system, the low oxygen

concentration and diffusion coefficient cause the deficient accessibility of photocatalyst to combine with oxygen. The solubility of oxygen in water is only 8 mg/L at room pressure and temperature [6,27,28], resulting in retarded kinetics of photocatalytic H₂O₂ formation. Secondly, the powder dispersed in the solution will cause unavoidable decomposition of the generated H₂O₂, resulting in a loss of overall output [29–32]. Despite great progress have made in photocatalyst development and design, one of the rate-limiting step that poor accessibility of the O₂ to photocatalysts in water remains largely unexplored.

To overcome the problem of mass transfer of oxygen, the great success of gas diffusion electrode in the application in electrocatalytic CO₂ reduction has inspired us to develop of the photocatalytic interface. In this work, we presented a tubular confined microenvironment in the superhydrophobic interface to enhance O₂ diffusion, and inhibit H₂O₂ decomposition. A loose, porous melamine foam (MF), coating through graphene and polytetrafluoroethylene (PTFE) to form a hydrophobic porous skeleton structure, is used as substrate. The gas will quickly transfer through the hydrophobic side into the reaction interface. The graphitic carbon nitride with Na doping and N defect (Na-CvCN), a high-performance 2e⁻ ORR catalyst in our previous report [33], is employed as a typical photocatalyst. Based on the results of scanning electron microscopy (SEM) and X-ray micro-computed tomography (Micro-CT), a

* Corresponding author at: Department of Environmental Science, Zhejiang University, Hangzhou, Zhejiang 310058, China.

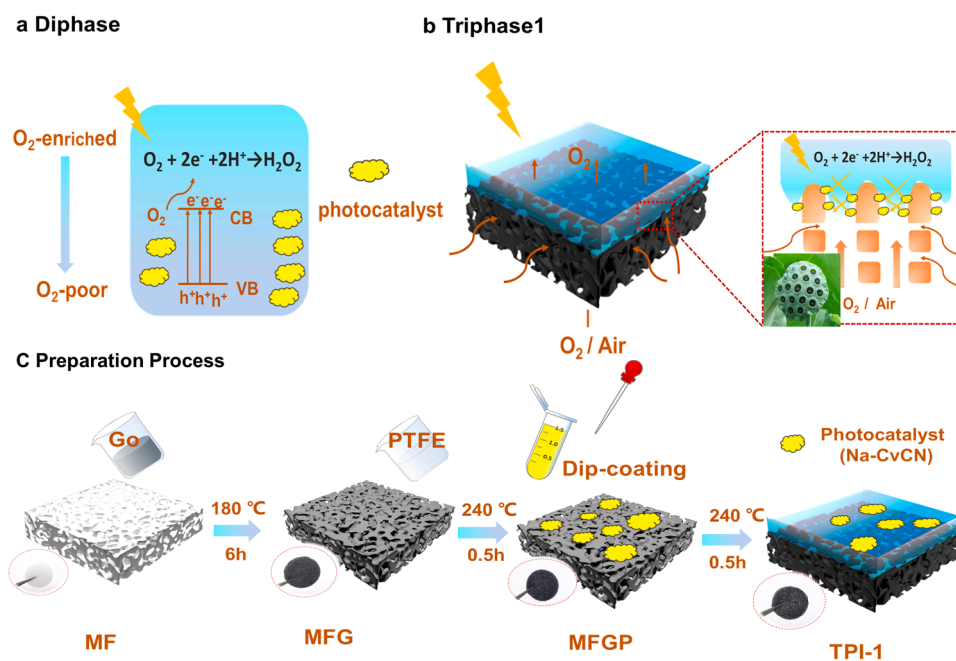
E-mail address: blchen@zju.edu.cn (B. Chen).

<https://doi.org/10.1016/j.apcatb.2022.121066>

Received 14 October 2021; Received in revised form 11 December 2021; Accepted 2 January 2022

Available online 5 January 2022

0926-3373/© 2022 Elsevier B.V. All rights reserved.



Scheme 1. Schematic illustration of Diphase and Triphase interface. (a) The conventional diphase reaction system; (b) Tubular confined microenvironment in super-hydrophobic reaction microenvironment; (c) Illustration of the TPI-1 fabrication process and the corresponding digital images, respectively. The concentration of GO and PTFE is 3 and 3 mg/mL, respectively.

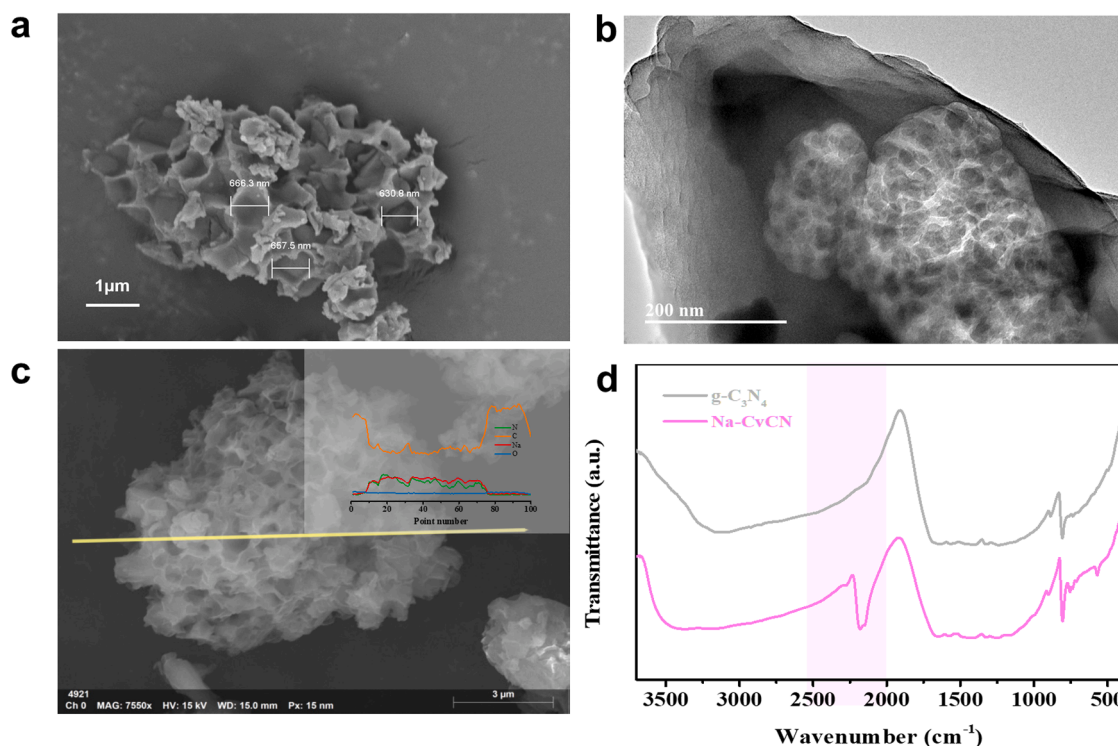


Fig. 1. The surface morphology and microstructure of Na-CvCN. The SEM (a) and TEM (b) images of Na-CvCN. (c) SEM image of Na-CvCN and corresponding element intensity along the yellow line (inset); (d) FTIR spectra of g-C₃N₄ and Na-CvCN.

hole-rich structure can be observed, which facilitates the rapid diffusion of air to the catalytic interface. Confocal laser scanning microscopy (CLSM) tests have shown that the Wenzel-Cassie state coexists in a hydrophobic interface and form a tubular confined space with a thickness of about 100 μm . In addition, H_2O_2 produced in the channel can spread rapidly into the aqueous solution, avoiding decomposition in contact with the catalyst, thus greatly reducing the decomposition coefficient.

This triphase system can provide more inspiration for the development of a high-efficient catalytic interface for photocatalytic reaction.

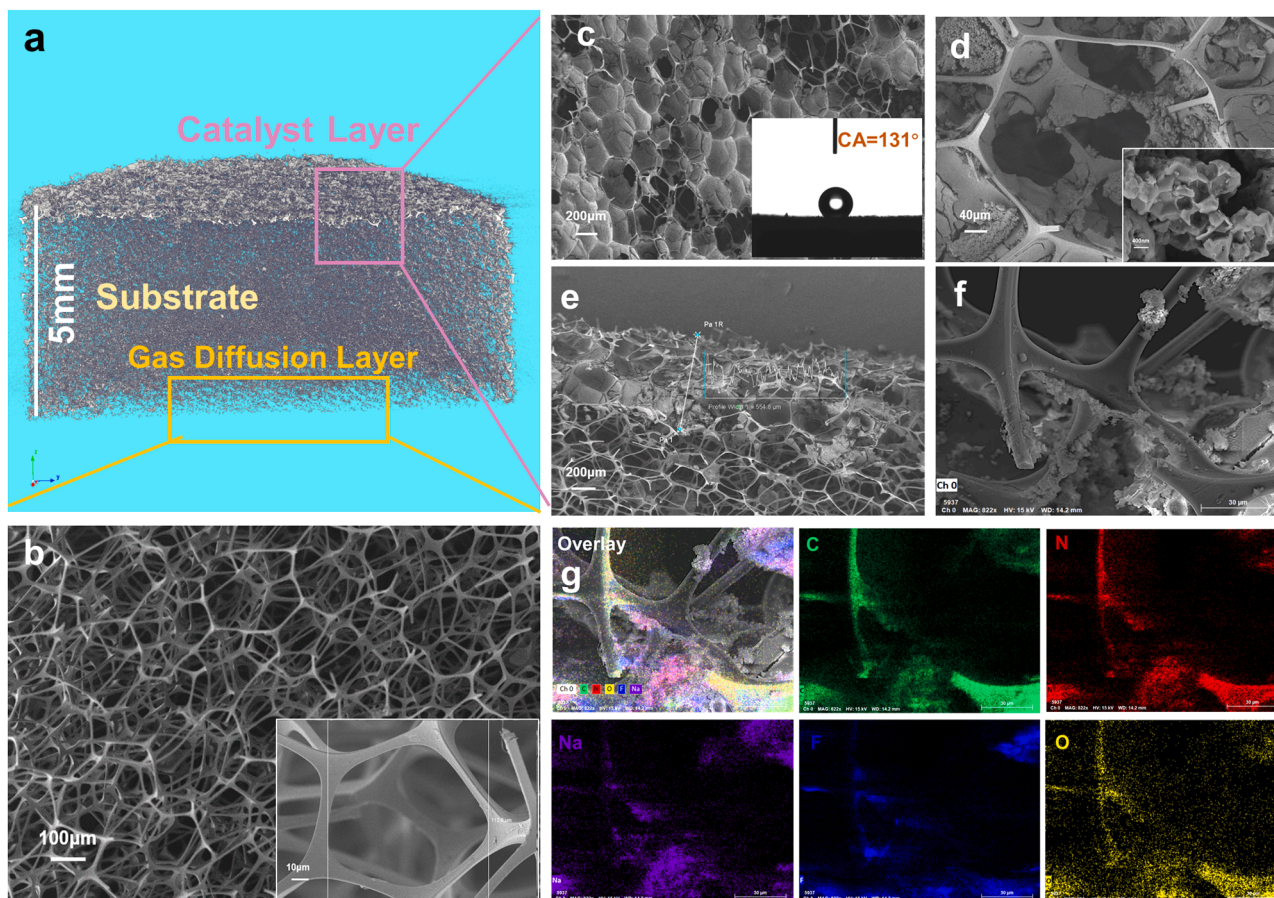


Fig. 2. The surface morphology and microstructure of the TPI-1. (a) The micro-CT image of Na-CvCN@MFPG; (b) The SEM images of MF and enlarge part (inset); (c) SEM image of MFPG and corresponding water contact angle (inset); (d) SEM image of the MFPG coated with Na-CvCN and the morphology of Na-CvCN (inset); (e) SEM image of cross-section of Na-CvCN@MFPG; (f, g) SEM image of Na-CvCN@MFPG and the corresponding element mapping.

2. Experimental section

2.1. Materials and characterization

All materials and chemical reagents were purchased commercially and used without further purification. Scanning electron microscopy (SEM) was performed on SU-8000 (Hitachi, Tokyo) to characterize the morphology of interface. X-ray diffraction (XRD) was measured on a Bruker D8 Advance with Cu K α radiation. UV-vis diffuse reflectance spectra (DRS) were conducted on a UV-vis spectrophotometer (Shimadzu, UV-2550) with BaSO₄ as a reference. Fourier transform infrared spectroscopy (FTIR, Thermo, America) was used to analyze the functional groups. X-ray photoelectron spectroscopy (XPS) was conducted on an Thermo Scientific K-Alpha+ (America) to analysis the surface chemical compositions. Water contact angle (WCA) were measured on an OSA Optical Surface Analyzer-OSA200-B. X-ray Micro-CT was used to analyze the internal composition of the substrate material. Confocal laser scanning microscopy (CLSM) (Zeiss LSM 880) was applied to observe the structure of TPI-1 interface.

2.2. Preparation of photocatalysts

The samples of g-C₃N₄ and Na-CvCN were synthesized following our previous reports, and the precursor dose and yield of catalysts are given in Table S1 (Supporting information) [33–35]. For g-C₃N₄, 10 g melamine was calcined at 550 °C for 4 h in the muffle with a ramp rate of 2.3 °C/min. And the resulting yellow solids was ground into powder and calcined at 500 °C for 2 h. As for Na-CvCN, 2 g DCDA and 10 g NaCl were dissolved in 100 mL of ultrapure water. After keeping stirring over

night, the mixture was frozen with liquid nitrogen and then freeze-dried to obtain white powder. The calcined process was as completed at 550 °C in Ar atmosphere for 4 h with a heating rate of 2.3 °C/min. The resulting yellow powder was finely ground and washed with water to remove any water-soluble impurities. After carefully washed, the product was vacuum dried (60 °C for 12 h). Since we have evaluated the photocatalytic H₂O₂ properties of Na-CvCN and g-C₃N₄ in our previous work [33], in this experiment, NaCv-CN was selected as the model photocatalyst.

2.3. Fabrication of triphase interface

The fabrication process of TPI-1 is shown in Scheme 1c, where the Na-CvCN was immobilized on the surface of modified melamine foam (MF, 5-mm thick). After ultrasonically cleaning in water and ethanol for 15 min, the cleaned MF was soaked in GO suspension (3 mg/mL) for 10 min, then taken out to dry at 180 °C for 6 h. The obtained rGO@MF (MFG) was soaked in PTFE suspension (3 mg/mL) for 5 min, and then calcined at 240 °C for 0.5 h to prepare PTFE coated rGO@MF(MFGP). Appropriate amount of Na-CvCN was ultrasonically dispersed in a mixture of water and ethanol (4:1 vol ratio) to form ink (5 mg/mL), and different amount ink (50, 100, and 150 μ L) was coated on the side of MFGP to form a catalytic layer. Finally, the Na-CvCN@MFGP was calcined at 240 °C for 0.5 h. The amount of Na-CvCN in the catalyst layer is calculated about 0.56 ± 0.03 mg when coating 100 μ L ink. Unless specifically mentioned in this article, this load amount is the default value. In order to make a detailed comparison, we have prepared another two different three-phase catalytic surface interfaces (Fig. S1). TPI-2 was prepared in the same way as TPI-1, the only difference was

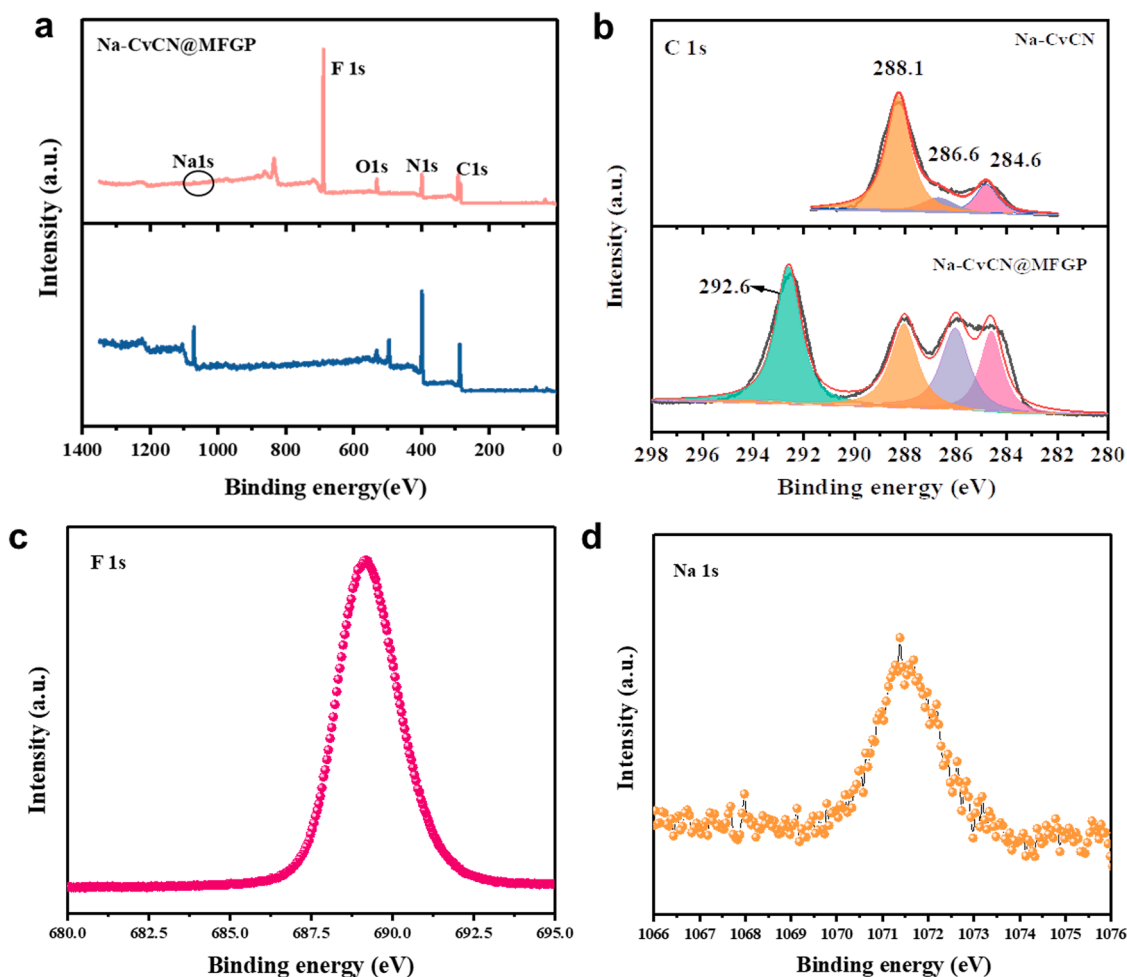


Fig. 3. The XPS survey spectra (a) of Na-CvCN and Na-CvCN@MFGP. The high resolution C1s spectra (b) of Na-CvCN and Na-CvCN@MFGP. The high resolution F1s (c) and Na 1s spectra (d) of Na-CvCN@MFGP.

that diffusion channel was blocked for experiment. TPI-3 (Fig. S2) was prepared in a similar way to TPI-1, the difference is that replacing MFGP with carbon fiber cloth, and the temperature of calcination changes to 360 °C.

2.4. Photocatalytic H_2O_2 production

The photocatalytic H_2O_2 generation were conducted in a homemade reactor (Fig. S3, 25 mm × 25 mm × 40 mm). 10 mL mixture (different ratios of ethanol and water) was used as reaction solution. The portion of TPI-1,2,3 that coated with Na-CvCN was immersed into reaction solution, while the other side (without Na-CvCN) was exposed to gas chamber. The default experimental state is that both the gas diffusion side and the solution side are exposed in the air. If necessary, N_2 or O_2 will be injected into gas chamber to change the atmosphere of the side of diffusion layer. It is noted that during the test of TPI-2, a rubber pad is required to block the channel between gas chamber and the MFGP. Control experiments based on a conventional two-phase system where the TPI-1 is completely submerged in water were also carried out. 300 W Xe lamp (equipped with AM 1.5 G) was used as a light resource. The concentration of H_2O_2 was determined by the N, N-diethyl-1,4-phenylenediamine (DPD) method.

3. Results and discussion

3.1. Characterization of triphase system

The graphitic carbon nitride with Na doping and N defect (Na-CvCN) is achieved by using NaCl as a hard template, after calcining the mixture of dimeric cyanamide (DCDA) and NaCl. SEM is firstly used to characterize the morphology of obtained photocatalysts. Na-CvCN shows a rich porous structure with a pore size of about 650 nm (Fig. 1a). The TEM image further shows that the honeycomb-like pore structure of Na-CvCN exists and the pore walls are about 2–5 nm (Fig. 1b). This unique hierarchical structure provides favorable conditions for the capture and diffusion of oxygen molecules on the surface of Na-CvCN [36]. Through SEM mapping analysis (Fig. 1c), the intensity of element C, N, O, Na increases with the yellow line across Na-CvCN (Fig. 1c inset). It is worth noting that there is no signal of Cl element, which indicates that Na element is successfully doped into the framework of g- C_3N_4 , not in the form of NaCl attached on the surface of g- C_3N_4 . Further, the X-ray diffraction (XRD) pattern of Na-CvCN exhibits distinctive changes compared to pristine g- C_3N_4 (Fig. S4). The intensity of (002) peak of Na-CvCN greatly decreases, and the (001) peak is disappeared, indicating the reaction of NaCl and DCDA during calcining process. In addition, the FTIR spectroscopy of Na-CvCN shows a new and strong peak appeared at 2180 cm^{-1} , which is attributed to the cyano group ($-\text{C}\equiv\text{N}$). This indicates that there is a defect of N in the structure of g- C_3N_4 , resulting in a cyano group. In our previous report, the interaction between Na doping and cyano group makes Na-CvCN superior

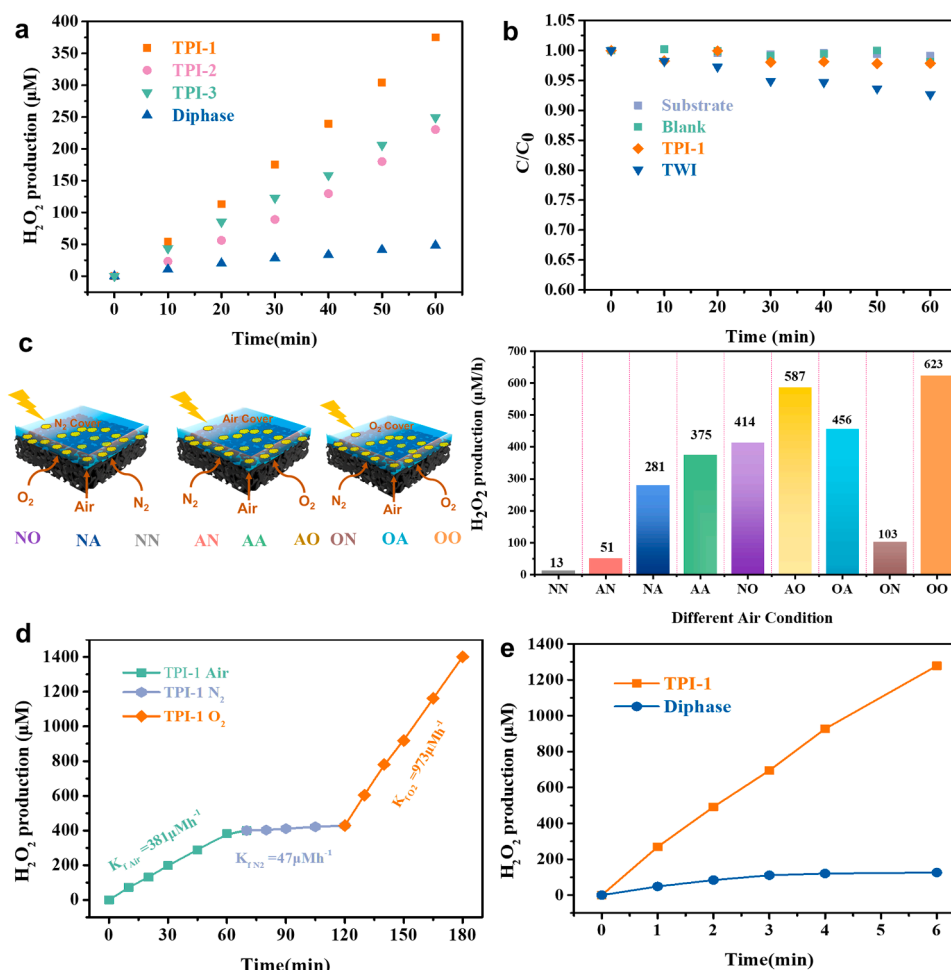


Fig. 4. (a) The photocatalytic generation of H₂O₂ over different system; (b) The photocatalytic decomposition of H₂O₂ over substrate, TPI-1, and TW1, C₀(H₂O₂) = 2 mM; (c) Photocatalytic generation H₂O₂ under different operational conditions, the right panel displays a schematic illustration of the nine operational conditions; (d) The photocatalytic generation of H₂O₂ during a long time; (e) The photocatalytic H₂O₂ over TPI-1 under continuous gas change experiments.

photocatalytic H₂O₂ generation performance [33].

X-ray Micro-CT is a powerful tool to analyze the inner space of a material. As presented in Fig. 2a, MF modified by GO and PTFE as the substrate and the diffusion layer, while Na-CvCN is loaded on the one side to form catalyst layer with abundant confined space. The gas diffusion layer is consisted of a loose skeleton and interconnected network with an inter distance of ~ 112 μm (Fig. 2b) and the porosity is higher than 99%. Thereby, the hindrance of oxygen mass transfer becomes pretty low, which allows O₂ spread directly to the reaction interface. In addition, after coating with rGO and treated by PTFE, the surface of MFGP still keep a high macroporosity (Fig. 2c) and have a stable superhydrophobicity interface with water contact angle (WCA) of 131° (Fig. 2c inset and Fig. S5). For the catalytic layer (Fig. 2d), Na-CvCN is firmly attached to the mesh structure of MFGP, a unique distribution that would make the photocatalyst to fully contact with the oxygen of the diffusion layer, thereby enhancing the performance of photocatalytic production of H₂O₂. Through the analysis of the cross-section (Fig. 2e), the thickness of the catalytic layer is about ~ 500 μm. Due to the interconnection of rGO, PTFE, and Na-CvCN, a rich confined microenvironment, conducive to oxygen reduction, was created. Elemental analysis mapping (Fig. 2f, g) also confirms the existence of this interconnection state, with elements such as C, N, O, Na, F presented an overlapping distribution states.

XPS was conducted to analyze the surface chemical compositions and further revealed the interaction between photocatalyst and gas diffusion layer. From the XPS survey (Fig. 3a) of Na-CvCN@MFGP and

Na-CvCN, elements such as C, N, O, and Na are clearly observed in both samples, while element F can only be found in the former, indicating the element F is from the PTFE coated on MFG. As for C1s of Na-CvCN (Fig. 3b), three distinctive peaks located at 284.6, 286.6, and 288.1 eV are corresponding to the carbon impurities (C-C), the C-NH_x group, and N=C-N in the plane of aromatic ring. Moreover, a strong and new peak at 292.6 eV was observed in Na-CvCN@MFGP. Further analysis on the element F (Fig. 3c), the strong peak at 689.6 eV can be ascribed to the F element in C-F structure. These analysis clearly indicates the successful modification of MFG via PTFE. Fig. 3d shows the high-resolution of Na 1s, and the peak at 1071.8 eV is a great indicator to evaluate the structural stability of the catalyst.

3.2. Photocatalytic H₂O₂ production on the triphase system

We firstly optimized the coating amount of different Na-CvCN and the concentration of the sacrificial agent ethanol. Fig. S6a shows the H₂O₂ production performance under different loading amount of Na-CvCN on catalyst layer. We can see that as the catalyst loading increases, the H₂O₂ activity was also increased. But it is worth noting that there is no great difference between the three loading. This is because the area of MFGP is relatively small, both the three different loading amounts of Na-CvCN can fully cover the catalytic surface. Therefore, we choose the catalyst of 100 μL as the default loading. We also test the photocatalytic H₂O₂ generation in solution with different concentration of ethanol. From the Fig. S6b, the concentration ratio of 0.5:9.5

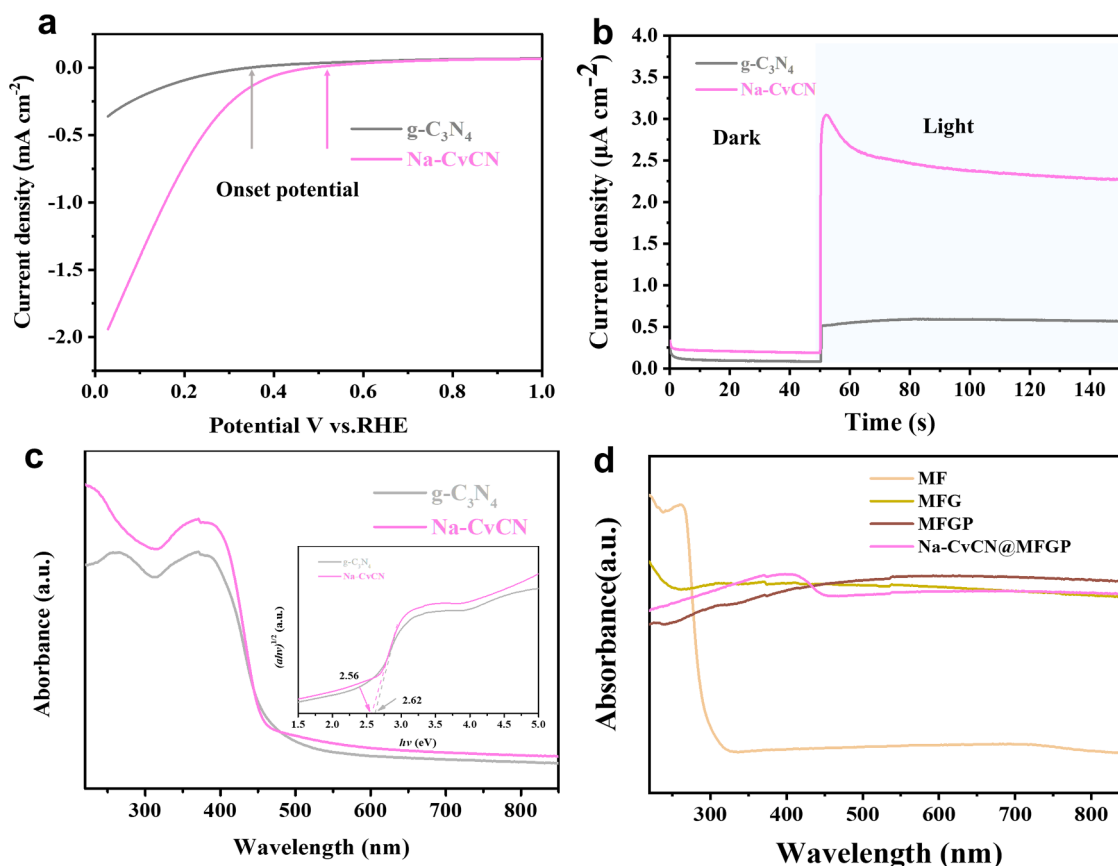


Fig. 5. (a) The linear scan curve of g-C₃N₄ and Na-CvCN measured at 1600 rpm on rotating disk electrode (Pine) under O₂ saturated Phosphate buffer (pH = 6.8); (b) The photocurrent curve of g-C₃N₄ and Na-CvCN electrode (coating on FTO glass) measured under 0.1 M Na₂SO₄ solution. UV-vis DRS spectra (c) and (c inset) corresponding plots of transformed Kubelka-Munk function vs. photo energy of g-C₃N₄ and Na-CvCN; The UV-vis DRS spectra (d) of MF, MFG, MFGP, and Na-CvCN@MFGP.

exhibited the best H₂O₂ yield rate (483 μM/h), and the H₂O₂ generated rate is similar in solution with 10% and 15% (~380 μM/h). Interestingly, the photocatalytic H₂O₂ performance in high EtOH concentration solution was decreased (240 μM/h), owing to the high concentration of ethanol solution can destroy the three-phase interface, more aqueous solution will penetrate into the catalytic layer, thereby reducing the three-phase interface and confined environment. Therefore, in order to have a good comparison with other benchmarks, we chose 10% ethanol concentration as the model experiment condition.

The performance of photocatalytic H₂O₂ generation over different interface systems were then measured (Fig. 4a). In all systems, the accumulated H₂O₂ concentration after 1 h reaction increased at a linear rate (zero-order kinetic), indicating that the oxygen concentration is sufficient to participate in the 2e⁻ ORR. The best H₂O₂ production rate (375 μM/h) is obtained over TPI-1, much higher than that in diphasic (48 μM/h). In fact, the measured concentration of H₂O₂ is determined by the rate constant of zero-order formation (K_f) and the first-order kinetics decomposition (K_d) of H₂O₂. The generation of H₂O₂ can be measured by the formula: $[H_2O_2] = (k_f/k_d)\{1 - \exp(-k_d t)\}$ [37–39]. According to the decomposition results (Fig. 4b), TPI-1 displays an extremely low K_d constant (0.02), much lower than that of the two-phase system, which are attributed to the unique microenvironment. In order to further explore the contribution of oxygen from the gas and water phase, the production of H₂O₂ under different gas atmospheres were measured in the TPI-1 system. The influence of gas in the diffusion layer on the reaction was investigated by introducing N₂ into the liquid phase to decrease the concentration of O₂ in reaction solution (Figs. 4c, and S7). When the gas diffusion layer is permeated with N₂ (NN), the formation of H₂O₂ is almost stagnated (13 μM/h). Air or O₂ is

injected into the gas diffusion layer (NA or NO), the reaction rates are greatly enhanced, which are 281 and 414 μM/h, respectively. When the reaction solution is returned to the air-saturated aqueous solution, the gas diffusion layer is covered with N₂ (AN), the formation rate of H₂O₂ is pretty low (51 μM/h), lower than that of air (AA, 375 μM/h), and O₂ (AO 587 μM/h) (Figs. 4c, and S8). Moreover, when O₂ is bubbled into the reaction solution, the gas diffusion layer is covered with N₂ (ON), the formation rate of H₂O₂ is also low (103 μM/h), lower than that of air (OA, 456 μM/h), and O₂ (OO, 623 μM/h). Continuous gas change experiments (Fig. 4d) also proved that the gas from the gas transport layer plays a key role in the reaction. When the reaction time was further extended to 6 h (Fig. 4e), we found that TPI-1 could still maintain a nearly linear growth rate, while the growth rate of H₂O₂ in diphasic was almost stagnated. The stagnated growth rates in diphasic system is belonging to the poor oxygen supply interface. In the diphasic system, the solubility of oxygen is very low (8 mg/L) at room temperature and pressure. In addition, the diffusion rate of O₂ in water to the Na-CvCN is pretty slow (2.1×10^{-5} cm² s⁻¹) [40]. While, in the triphase, O₂ can be rapidly transferred through the hydrophobic diffusion layer to the surface of Na-CvCN to participate in the oxygen reduction reaction with a diffusion rate of 2.0×10^{-1} cm² s⁻¹, much faster than that in water. Based on the above control experiments and long-term test, the following conclusions can be obtained: (1) the H₂O₂ was generated through oxygen reduction process rather than others; (2) O₂ consumed at Na-CvCN surface was quickly resupplied through gas diffusion layer side; (3) the contribution of O₂ in the gas diffusion layer to the overall production of H₂O₂ was dominant. The production rate of H₂O₂ at different wavelengths were also investigated (Fig. S9). As the wavelength increases, the production rate of H₂O₂ decreases, indicating that

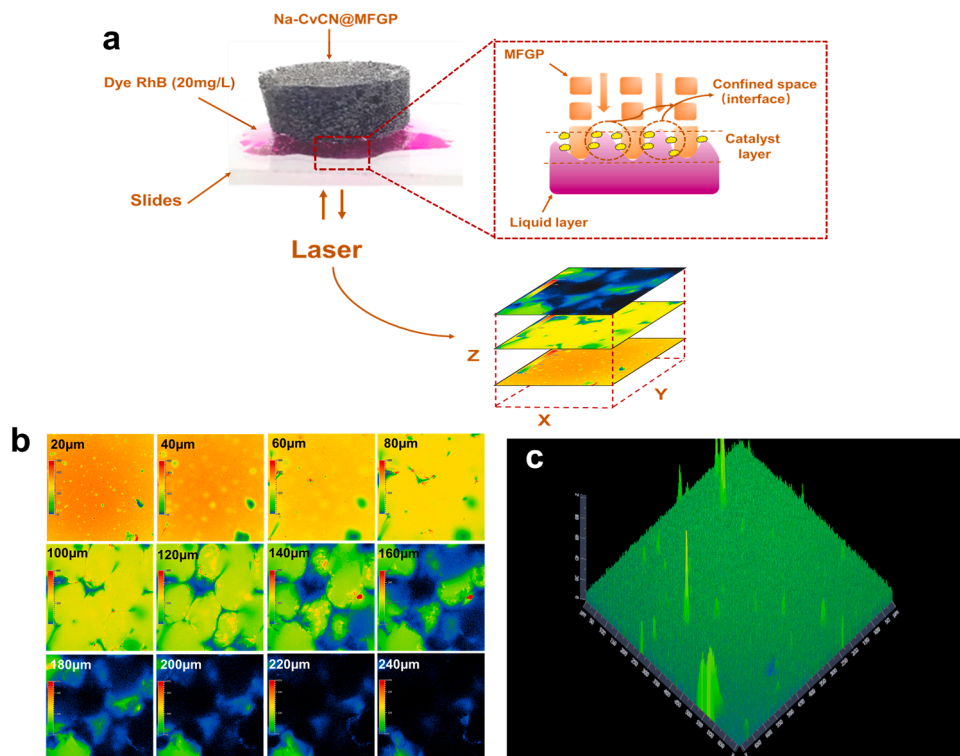


Fig. 6. (a) Schematic illustration of the method used to investigate the triphase interface by confocal laser scanning microscopy (excited at 561 nm); (b) The cross-sectional fluorescence images along the z axis; (c) Confocal 3D reconstruction image of (b) the solid-liquid-gas interface (RhB liquid droplet on the surface of MFGP).

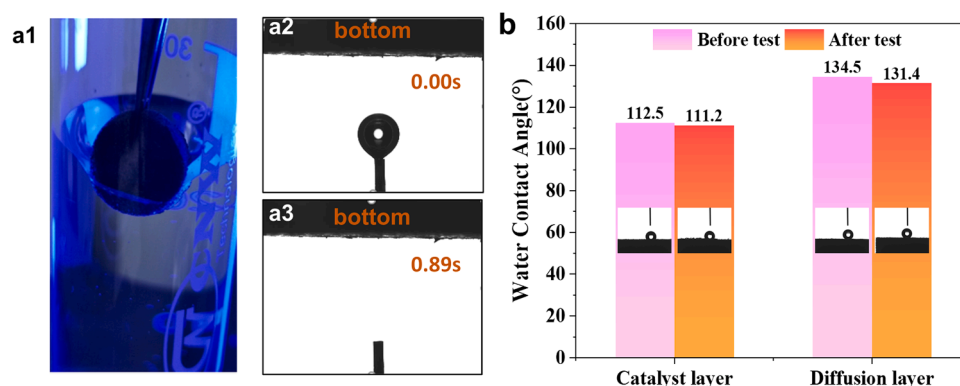


Fig. 7. (a1) picture of the Na-CvCN@MFGP immersed into water by an external force; (a2, a3) the gas contact angle at the bottom of the Na-CvCN@MFGP (diffusion layer) measured underwater; (b) The WCA of catalyst layer and diffusion layer before and after 6 h photocatalytic H_2O_2 generation test and corresponding WCA images.

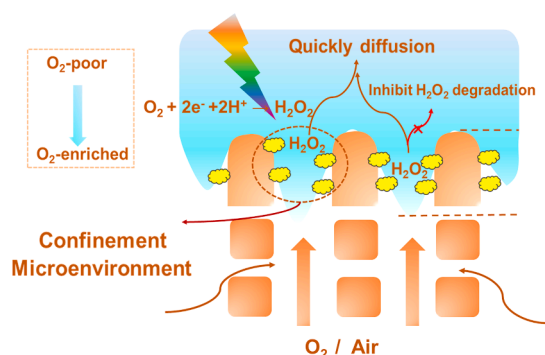


Fig. 8. The illustration of solid-liquid-gas triphase interface with tubular confined microenvironment for photocatalytic H_2O_2 generation.

the photocatalytic activity in the visible light region needs to be further studied.

The stability of the catalyst is very important for the photocatalytic reaction. Therefore, the cycling tests of photocatalytic H_2O_2 generation over Na-CvCN@MFGP under TPI-1triphase were also measured (Fig. S10a). After ten cycles, Na-CvCN@MFGP system still showed an excellent H_2O_2 production rate ($312 \mu\text{M/h}$), indicating a good stability. Fourier transform infrared spectroscopy analysis of Na-CvCN on the surface of MFGP showed that the cyano group defects located at 2180 cm^{-1} still existed stably before and after the reaction (Fig. S10b). At the same time, XPS spectrum was also performed to reveal the surface elements of reaction interface. As shown in the Fig. S10c, the peak at 689.6 eV can be ascribed to the F element in C-F structure, which indicates that the PTFE molecules at the interface are stable to the support the three-phase interface. The peak at 1071.8 eV is corresponded to the Na element in Na-CvCN (Fig. S10d). Therefore, Na element was also

stable before and after test, although the Na content on the catalyst surface was very low.

3.3. Mechanism insights

The rotating disk electrode test is an effective method to monitor the oxygen reduction process. We tested the linear scan curves of Na-CvCN and g-C₃N₄ at 1600 rpm under O₂ saturated Phosphate buffer (pH = 6.8). As shown in the Fig. 5a, the onset potential of Na-CvCN is 20 mV higher than that of pure g-C₃N₄. The current density of Na-CvCN is also significantly higher than that of g-C₃N₄, indicating that Na-CvCN has an excellent oxygen reduction ability. In addition, the photocurrent of Na-CvCN exhibited a more strong and distinctive photocurrent than g-C₃N₄. The above results shows that Na-CvCN as a photocatalyst has excellent photo-generated charge separation ability, and can efficiently reduce oxygen to further produce H₂O₂. To understand the key role of triphase interface, we then explored the light absorption properties of the interface. From the UV-vis DRS of g-C₃N₄ and Na-CvCN, the absorption range of Na-CvCN has increased significantly (Fig. 5c), which means that the band gap has narrowed (Fig. 5c inset). This is due to the change in the molecular structure of g-C₃N₄ [33]. Fig. 5d shows the light absorption characteristics of the substrates. It can be found that the initial MF has a weak light absorption ability between 325 and 820 nm. After coating a layer of rGO and PTFE, the light absorption ability of MFGP is greatly enhanced. The strong light absorption capacity of the substrate enables the loaded Na-CvCN to make full use of solar energy to generate photo-generated electrons.

Fig. 6a shows the schematic illustration of the CLSM analysis of the catalyst layer. Na-CvCN is placed inverted on rhodamine B(RhB) solution with fluorescence. The penetration depth and cover information of RhB into the catalytic interface along the Z axis can be directly observed through the reconstruction of the tomography images to form a three-dimensional graph. As seen in Fig. 6b, the color changes from bright red to green refers to the changes of fluorescence intensity from strong to weak. The cross-sectional fluorescence images along the z axis at 40 μm still shows bright red, indicating occupied by the luminous solution. At the z-axis position of 80–220 μm, a distinctly non-continuous interface appears, indicating the coexistence interface of Cassie-Wenzel coexistence state (Fig. S11), which is considered as the ideal triphase structure for O₂ supply form air to Na-CvCN. In addition, the color darkens or even disappears from bright green, indicating that the penetration of the luminous solution becomes weaker and even disappears. At the z-axis position of 240 μm, a large, dark non-fluorescent area appears, indicating that the RhB cannot penetrate this depth. Interestingly, from the 3D reconstruction image (Fig. 6c), it can be found that the penetration path of solution is a tubular structure. Thus it can be assumed that the micro-environment in which oxygen reduction to generate H₂O₂ occurs is in a confined space of tubular-like. In this micro-environment, oxygen is quickly involved in the interface reaction through the gas diffusion layer to generate high concentrations of H₂O₂ and then the generated H₂O₂ will rapidly spreading to low-concentration reaction solutions, which fully suppress the decomposition of H₂O₂.

The stability of the three-phase catalytic interface is essential for the continuous photocatalytic reaction. The wettability-controlled structure of TPI-1 interfaces was further investigated. The hydrophobicity of the side of Na-CvCN@MFGP can be observed in Fig. 7a1. When immersing the Na-CvCN@MFGP into water by external force, a nonwetting Cassie-Baxter interface generated between the sponge and the surrounding water owing to the entrapped air residing in the rough surface of the Na-CvCN@MFGP [41]. The ability of the gas diffusion layer to entrap gas in the water was measured by the underwater gas contact angle, as shown in Fig. 7a1 and a2. The bottom of Na-CvCN@MFGP (diffusion layer) can quickly capture the gas in the water within a second, indicating a superhydrophobic surface and powerful ability of gas diffusion. The stable wettability of the catalytic interface is extremely important for maintaining the gas-liquid-solid three-phase catalytic reaction interface.

The water contact angle of NaCvCN-MFGP were measured before and after photocatalytic production of H₂O₂ (6 h). It can be seen that before and after the reaction, both the catalytic layer and the gas diffusion layer exhibit a stable water contact angle (Fig. 7b), indicating a stable gas-liquid-solid three-phase catalytic reaction. The WCA of catalyst layer was slightly decreased to 111.2° from 112.5°, and the WCA of the gas diffusion layer was also decreased slightly, indicating the stabilizing of triphase interface.

4. Conclusion

Accordingly, a solid-liquid-gas triphase interface with tubular confined microenvironment was successfully applied to enhance the photocatalytic H₂O₂ generation and inhibit H₂O₂ decomposition (Fig. 8). The gas diffusion layer, formed by coating rGO and PTFE on melamine foam, has a high porosity (99%), which allows the O₂ in the air can be quickly transferred to the catalytic layer, greatly boosting the oxygen concentration on the surface of the catalyst. At the same time, the formation of tubular confined space in the catalyst layer not only can ensure adequate light absorption but also greatly inhibit the decomposition of H₂O₂. Our results show that the overall reaction activity can be significantly improved by the micro-environment engineering (wettability and architecture). It is hoped that the results of this work can provide new ideas and methods for the application of three-phase systems to photocatalytic H₂O₂ generation.

CRedit authorship contribution statement

Lei Chen: Methodology, Investigation, Data curation, Formal analysis, Writing – original draft. **Shan Li, Zhi Yang, and Cheng Chen:** Writing – review & editing, Investigation, Formal analysis. **Chiheng Chu:** Writing – review & editing, Formal analysis. **Baoliang Chen:** Conceptualization, Methodology, Writing – review & editing, Supervision, Funding acquisition.

Declaration of Competing Interest

The authors declare that they have no known competing financial interests or personal relationships that could have appeared to influence the work reported in this paper.

Acknowledgements

This project was supported by the National Natural Science Foundation of China (Grants 21621005, and 21537005), and the National Key Technology Research and Development Program of China (Grant 2018YFC1800705).

Appendix A. Supporting information

Supplementary data associated with this article can be found in the online version at doi:10.1016/j.apcatb.2022.121066.

References

- [1] J.M. Campos-Martin, G. Blanco-Brieva, J.L.G. Fierro, Hydrogen peroxide synthesis: an outlook beyond the anthraquinone process, *Angew. Chem. Int. Ed.* 45 (2006) 6962–6984.
- [2] J. Xu, C. Zhu, S. Song, Q. Fang, J. Zhao, Y. Shen, A nanocubicle-like 3D adsorbent fabricated by in situ growth of 2D heterostructures for removal of aromatic contaminants in water, *J. Hazard. Mater.* 423 (2022), 127004.
- [3] J. Ma, K. Wang, C. Wang, X. Chen, W. Zhu, G. Zhu, W. Yao, Y. Zhu, Photocatalysis-self-Fenton system with high-fluent degradation and high mineralization ability, *Appl. Catal. B: Environ.* 276 (2020), 119150.
- [4] H. Hou, X. Zeng, X. Zhang, Production of hydrogen peroxide by photocatalytic processes, *Angew. Chem. Int. Ed.* 59 (2020) 17356–17376.
- [5] Y. Zhao, P. Zhang, Z. Yang, L. Li, J. Gao, S. Chen, T. Xie, C. Diao, S. Xi, B. Xiao, C. Hu, W. Choi, Mechanistic analysis of multiple processes controlling solar-driven

- H₂O₂ synthesis using engineered polymeric carbon nitride, *Nat. Commun.* 12 (2021) 3701.
- [6] S. Yang, A. Verdaguer-Casadevall, L. Arnarson, L. Silvioli, V. Čolić, R. Frydendal, J. Rossmeisl, I. Chorkendorff, I.E.L. Stephens, Toward the decentralized electrochemical production of H₂O₂: a focus on the catalysis, *ACS Catal.* 8 (2018) 4064–4081.
 - [7] X. Li, B. Kang, F. Dong, Z. Zhang, X. Luo, L. Han, J. Huang, Z. Feng, Z. Chen, J. Xu, B. Peng, Z.L. Wang, Enhanced photocatalytic degradation and H₂/H₂O₂ production performance of S-pCN/WO_{2.72} S-scheme heterojunction with appropriate surface oxygen vacancies, *Nano Energy* 81 (2021), 105671.
 - [8] Q. Zhang, X. Liu, M. Chaker, D. Ma, Advancing graphitic carbon nitride-based photocatalysts toward broadband solar energy harvesting, *ACS Mater. Lett.* 3 (2021) 663–697.
 - [9] Z. Jin, Y. Liu, L. Wang, C. Wang, Z. Wu, Q. Zhu, L. Wang, F.-S. Xiao, Direct synthesis of pure aqueous H₂O₂ solution within aluminosilicate zeolite crystals, *ACS Catal.* 11 (2021) 1946–1951.
 - [10] Z. Zhou, B. Li, X. Liu, Z. Li, S. Zhu, Y. Liang, Z. Cui, S. Wu, Recent progress in photocatalytic antibacterial, *ACS Appl. Bio Mater.* 4 (2021) 3909–3936.
 - [11] J. Xiao, Q. Liu, M. Song, X. Li, Q. Li, J.K. Shang, Directing photocatalytic pathway to exceedingly high antibacterial activity in water by functionalizing holey ultrathin nanosheets of graphitic carbon nitride, *Water Res.* 198 (2021), 117125.
 - [12] Y. Yi, L. Wang, G. Li, H. Guo, A review on research progress in the direct synthesis of hydrogen peroxide from hydrogen and oxygen: noble-metal catalytic method, fuel-cell method and plasma method, *Catal. Sci. Technol.* 6 (2016) 1593–1610.
 - [13] H. Hou, X. Zeng, X. Zhang, Production of hydrogen peroxide by photocatalytic processes, *Angew. Chem. Int. Ed. Engl.* 59 (2020) 17356–17376.
 - [14] J. Zhang, J. Lang, Y. Wei, Q. Zheng, L. Liu, Y.-H. Hu, B. Zhou, C. Yuan, M. Long, Efficient photocatalytic H₂O₂ production from oxygen and pure water over graphitic carbon nitride decorated by oxidative red phosphorus, *Appl. Catal. B: Environ.* 298 (2021), 120522.
 - [15] Y.X. Ye, J. Pan, F. Xie, L. Gong, S. Huang, Z. Ke, F. Zhu, J. Xu, G. Ouyang, Highly efficient photosynthesis of hydrogen peroxide in ambient conditions, *Proc. Natl. Acad. Sci. USA* 118 (2021), e2103964118.
 - [16] S. Wu, H. Yu, S. Chen, X. Quan, Enhanced photocatalytic H₂O₂ production over carbon nitride by doping and defect engineering, *ACS Catal.* 10 (2020) 14380–14389.
 - [17] Y.-X. Ye, C. Wen, J. Pan, J.-W. Wang, Y.-J. Tong, S. Wei, Z. Ke, L. Jiang, F. Zhu, N. Zhou, M. Zhou, J. Xu, G. Ouyang, Visible-Light driven efficient overall H₂O₂ production on modified graphitic carbon nitride under ambient conditions, *Appl. Catal. B: Environ.* 285 (2021), 119726.
 - [18] J. Cao, Q. Wu, Y. Zhao, K. Wei, Y. Li, X. Wang, F. Liao, H. Huang, M. Shao, Y. Liu, Z. Kang, In-situ photovoltage transients assisted catalytic study on H₂O₂ photoproduction over organic molecules modified carbon nitride photocatalyst, *Appl. Catal. B: Environ.* 285 (2021), 119817.
 - [19] Z. Wei, M. Liu, Z. Zhang, W. Yao, H. Tan, Y. Zhu, Efficient visible-light-driven selective oxygen reduction to hydrogen peroxide by oxygen-enriched graphitic carbon nitride polymers, *Energy Environ. Sci.* 11 (2018) 2581–2589.
 - [20] P. Zhang, Y. Tong, Y. Liu, J.J.M. Vequizo, H. Sun, C. Yang, A. Yamakata, F. Fan, W. Lin, X. Wang, W. Choi, Heteroatom dopants promote two-electron O₂ reduction for photocatalytic production of H₂O₂ on polymeric carbon nitride, *Angew. Chem. Int. Ed. Engl.* 59 (2020) 16209–16217.
 - [21] L. Zhou, J. Lei, F. Wang, L. Wang, M.R. Hoffmann, Y. Liu, S.-I. In, J. Zhang, Carbon nitride nanotubes with in situ grafted hydroxyl groups for highly efficient spontaneous H₂O₂ production, *Appl. Catal. B: Environ.* 288 (2021), 119993.
 - [22] H. Shi, Y. Li, X. Wang, H. Yu, J. Yu, Selective modification of ultra-thin g-C₃N₄ nanosheets on the (110) facet of Au/BiVO₄ for boosting photocatalytic H₂O₂ production, *Appl. Catal. B: Environ.* 297 (2021), 120414.
 - [23] Y. Xie, Y. Li, Z. Huang, J. Zhang, X. Jia, X.-S. Wang, J. Ye, Two types of cooperative nitrogen vacancies in polymeric carbon nitride for efficient solar-driven H₂O₂ evolution, *Appl. Catal. B: Environ.* 265 (2020), 118581.
 - [24] Y. Shiraishi, Y. Kofuji, H. Sakamoto, S. Tanaka, S. Ichikawa, T. Hirai, Effects of surface defects on photocatalytic H₂O₂ production by mesoporous graphitic carbon nitride under visible light irradiation, *ACS Catal.* 5 (2015) 3058–3066.
 - [25] J. Xiong, X. Li, J. Huang, X. Gao, Z. Chen, J. Liu, H. Li, B. Kang, W. Yao, Y. Zhu, CN/rGO@BPQDs high-low junctions with stretching spatial charge separation ability for photocatalytic degradation and H₂O₂ production, *Appl. Catal. B: Environ.* 266 (2020), 118602.
 - [26] X. Wang, K. Maeda, A. Thomas, K. Takanabe, G. Xin, J.M. Carlsson, K. Domen, M. Antonietti, A metal-free polymeric photocatalyst for hydrogen production from water under visible light, *Nat. Mater.* 8 (2009) 76–80.
 - [27] Q. Zhang, M. Zhou, G. Ren, Y. Li, Y. Li, X. Du, Highly efficient electrosynthesis of hydrogen peroxide on a superhydrophobic three-phase interface by natural air diffusion, *Nat. Commun.* 11 (2020) 1731.
 - [28] Y. Wang, R. Shi, L. Shang, G.I.N. Waterhouse, J. Zhao, Q. Zhang, L. Gu, T. Zhang, High-efficiency oxygen reduction to hydrogen peroxide catalyzed by nickel single-atom catalysts with tetradentate N₂O₂ coordination in a three-phase flow cell, *Angew. Chem. Int. Ed.* 59 (2020) 13057–13062.
 - [29] Y. Shiraishi, S. Kanazawa, Y. Kofuji, H. Sakamoto, S. Tanaka, T. Hirai, Sunlight-driven hydrogen peroxide production from water and molecular oxygen by metal-free photocatalysts, *Angew. Chem. Int. Ed. Engl.* 53 (2014) 13454–13459.
 - [30] Y. Shiraishi, S. Kanazawa, Y. Sugano, D. Tsukamoto, H. Sakamoto, S. Ichikawa, T. Hirai, Highly selective production of hydrogen peroxide on graphitic carbon nitride (g-C₃N₄) photocatalyst activated by visible light, *ACS Catal.* 4 (2014) 774–780.
 - [31] Y. Kofuji, Y. Isobe, Y. Shiraishi, H. Sakamoto, S. Tanaka, S. Ichikawa, T. Hirai, Carbon nitride-aromatic diimide-graphene nanohybrids: metal-free photocatalysts for solar-to-hydrogen peroxide energy conversion with 0.2% efficiency, *J. Am. Chem. Soc.* 138 (2016) 10019–10025.
 - [32] X. Zeng, Y. Liu, Y. Kang, Q. Li, Y. Xia, Y. Zhu, H. Hou, M.H. Uddin, T. R. Gengenbach, D. Xia, C. Sun, D.T. McCarthy, A. Deletic, J. Yu, X. Zhang, Simultaneously tuning charge separation and oxygen reduction pathway on graphitic carbon nitride by polyethylenimine for boosted photocatalytic hydrogen peroxide production, *ACS Catal.* 10 (2020) 3697–3706.
 - [33] L. Chen, C. Chen, Z. Yang, S. Li, C. Chu, B. Chen, Simultaneously tuning band structure and oxygen reduction pathway toward high-efficient photocatalytic hydrogen peroxide production using cyano-rich graphitic carbon nitride, *Adv. Funct. Mater.* n/a (2021), 2105731.
 - [34] L. Chen, Y. Xu, B. Chen, In situ photochemical fabrication of CdS/g-C₃N₄ nanocomposites with high performance for hydrogen evolution under visible light, *Appl. Catal. B: Environ.* 256 (2019), 117848.
 - [35] L. Chen, Y. Xu, Z. Yang, K. Zhang, B. Chen, Cobalt (II)-based open-framework systems constructed on g-C₃N₄ for extraordinary enhancing photocatalytic hydrogen evolution, *Appl. Catal. B: Environ.* 277 (2020), 119207.
 - [36] M. Groenewolt, M. Antonietti, Synthesis of g-C₃N₄ nanoparticles in mesoporous silica host matrices, *Adv. Mater.* 17 (2005) 1789–1792.
 - [37] H. Zhang, L. Jia, P. Wu, R. Xu, J. He, W. Jiang, Improved H₂O₂ photogeneration by KOH-doped g-C₃N₄ under visible light irradiation due to synergistic effect of N defects and K modification, *Appl. Surf. Sci.* 527 (2020), 146584.
 - [38] C. Feng, L. Tang, Y. Deng, J. Wang, Y. Liu, X. Ouyang, H. Yang, J. Yu, J. Wang, A novel sulfur-assisted annealing method of g-C₃N₄ nanosheet compensates for the loss of light absorption with further promoted charge transfer for photocatalytic production of H₂ and H₂O₂, *Appl. Catal. B: Environ.* 281 (2021), 119539.
 - [39] Y. Wang, D. Meng, X. Zhao, Visible-light-driven H₂O₂ production from O₂ reduction with nitrogen vacancy-rich and porous graphitic carbon nitride, *Appl. Catal. B: Environ.* 273 (2020), 119064.
 - [40] Z. Liu, X. Sheng, D. Wang, X. Feng, Efficient hydrogen peroxide generation utilizing photocatalytic oxygen reduction at a triphase interface, *iScience* 17 (2019) 67–73.
 - [41] C. Chen, X. Zhu, B. Chen, Durable superhydrophobic/superoleophilic graphene-based foam for high-efficiency oil spill cleanups and recovery, *Environ. Sci. Technol.* 53 (2019) 1509–1517.